Plasma Sources Science and Technology

PAPER

# Predictive modeling of plasmas for gaseous plasmonics

To cite this article: David R Biggs *et al* 2018 *Plasma Sources Sci. Technol.* **27** 075005



IOP Publishing Plasma Sources Science and Technology
Plasma Sources Sci. Technol. **27** (2018) 075005 (12pp) https://doi.org/10.1088/1361-6595/aacd70

# Predictive modeling of plasmas for gaseous plasmonics

**David R Biggs, Thomas C Underwood and Mark A Cappelli**

Mechanical Engineering Department, Stanford University, Stanford, CA 94305, United States of America

E-mail: buggs@stanford.edu

Received 7 February 2018, revised 5 June 2018
Accepted for publication 19 June 2018
Published 6 July 2018


**Abstract**

The electromagnetic response of a resonant cavity in the presence of plasma discharges is studied, and a model to predict the formation of microwave pulses is developed using fluid plasma simulations and analytic microwave theory. Results for a 14 GHz rectangular cavity partially filled with plasma are then presented from both the model and from experiment as validation. Experimental results are shown to have good agreement with predicted values. It is seen that microwave pulses are generated with widths and delays as short as 1 $\mu$s during the plasma discharge decay and pulses with widths and delays as short as hundreds of ns during the plasma discharge ionization. Lastly, comparison is made with a simplified analysis by assuming a uniform plasma cylinder, which is shown to have reasonable agreement given enough fitting parameters.

Keywords: gas discharges, plasma modeling, electromagnetic wave control, resonant cavities, numerical methods

## 1. Introduction

There has been a resurgence of interest in the use of plasmas as active elements in microwave and terahertz systems to create tunable and reconfigurable devices, or for use in high power and harsh environments not suitable for conventional electronics. These devices can be realized in a variety of forms; microwave waveguide components [1, 2], photonic crystals [3–6], metamaterials [7, 8], or other forms of resonator arrays [9]. Plasmas may comprise anywhere from single elements to the entire structure of the system, but central to utilizing the plasma elements for high frequency applications is a requirement to understand the behavior and mechanics of the plasma. Diagnostic experimental methods give insight into the plasma behavior, but are generally limited to measurements of indirect or bulk properties and do not give a complete picture of the plasma system [10, 11]. What is required instead are numerical tools to adequately simulate the plasma behavior in space and time, which can then be independently validated by experimental means.

It is important to be cognizant of the plasma regime of interest, which is the low pressure glow discharge for electromagnetic devices with wave frequencies of tens to hundreds of GHz. This is due to the requirement that the electrons within the plasma be allowed to respond freely to electromagnetic waves and not be thwarted by excessive collisions with other particles. The latter results in energy transfer away from the electromagnetic wave and towards gas heating, in a form of Ohmic loss and wave damping. The simplest way of lowering the collision frequency is by lowering the gas pressure so that on average the electrons oscillate many times with the waves before encountering another particle through a collision.

The often used Drude model for the plasma dielectric constant, $\varepsilon_p$, is described by

$$\varepsilon_p = 1 - \frac{\omega_p^2}{\omega^2 + i\omega\nu_e}, \tag{1}$$

and depends on the wave frequency $\omega$, electron collision frequency $\nu_e$, and the plasma frequency

$$\omega_p = \sqrt{\frac{e^2 n_e}{m_e \varepsilon_0}}, \tag{2}$$

which is the fundamental parameter that determines a plasma's response to electromagnetic radiation. Here, $n_e$, $e$, and $m_e$ represent the electron number density, charge, and mass, and $\varepsilon_0$ is the permittivity of free space. The plasma dielectric constant is always less than one, implying that electromagnetic wavelengths

 

contract or are evanescent while within the plasma. Conversely, within resonators defined by a fixed scale or volume, wavelengths conform to that scale and electromagnetic modes increase in frequency. We exploit this plasma property to develop tunable and reconfigurable devices.

The numerical simulations of plasmas can be categorized in increasing stringency of continuum assumptions. Foremost and most basic, particle in cell methods capture plasma motion at a molecular level through direct numerical simulation at a large computational cost [12, 13]. They are typically used for the study of fundamental plasma properties and interactions with waves and instabilities, but do not scale to physically realizable systems in the laboratory. Next, Boltzmann methods decrease the computational cost by assuming a particle continuum with an arbitrary distribution function over velocity and physical space [14, 15]. These methods are useful for capturing the physics of non-ideal and highly non-equilibrium plasma conditions, but at the cost of high dimensionality. Thirdly, fluid models make simplifications by assuming velocity distribution functions to reduce the dimensionality and computational cost to levels appropriate for modeling laboratory gaseous discharges [16–19]. Non-equilibrium effects are approximated by solving the Boltzmann equation *a priori* for transport coefficients so that the assumed distribution function is not limited to a Maxwellian distribution [20].

A characteristic of glow discharges is that they have a region of large space charge in the vicinity of the electrodes (plasma sheath) with a length scale not insignificant of the total plasma discharge length [10]. Furthermore, the particles are accelerated within the sheath and in doing so drive the physics and structure of the plasma [21]. Although kinetic models are required to fully model sheath behavior [22], fluid models are often sufficient for capturing bulk properties such as particle density profiles for the application of electromagnetic wave interactions [23, 24].

Some recent numerical simulations have been carried out to study electromagnetic control with plasmas, such as with particle in cell simulations of nanosecond microdischarges for optical switching [25]. Other authors have used fluid models to study the resonant interactions of a single micro-plasma with high frequency electromagnetic waves [24], the limitations of different model approximations for plasmas in resonant structures [26], and the ensemble effect of arrays of microdischarges at controlling the propagation of microwaves through rectangular waveguides [27].

Still, there is the tendency in the gaseous plasmonics community to assume simplifications such as uniform plasma properties in order to draw conclusions from experiment or theory [5, 28–30]. While these methods might be attractive for first order analyses, they do not have high degrees of accuracy. Furthermore, when such assumptions are applied to analyze experimental data, the result is a reliance on over-fitting parameters that cannot be extrapolated for predictive purposes. Therefore, there is a need to have modeling of high fidelity to study complicated electromagnetic-plasma structures to make reliably predictions for the research and development of gaseous plasmonic devices.

In this paper we present a fluid model to simulate to high fidelity various plasma discharges suitable for electromagnetic control applications. We then present theory to predict the electromagnetic response of resonant structures in the presence of the simulated plasma discharges. Next, we outline our experimental setup for collecting data in a laboratory setting for validating and comparing with our modeling efforts. We presenting numerical results of a quasi-steady plasma discharge and pulsed plasma discharge, and compare our transient results with experimental data. Following this, we compare our simulated plasma properties with an analysis of what we would have predicted if we had assumed uniform plasma properties. Lastly, we draw conclusions about the applicability of these discharges and recommend areas for further investigation.

## 2. Methods

### 2.1. Model description

We describe here the fluid model used to simulate low temperature plasma discharges. The charged particle densities are governed by the continuity equation for species $p$

$$\frac{\partial}{\partial t} n_\mathrm{p} + \nabla \cdot \mathbf{\Gamma}_\mathrm{p} = \sum_r K_\mathrm{r} n_\mathrm{p} n_\mathrm{r}, \tag{3}$$

where $n_\mathrm{p}$ is the particle density, $\Gamma_\mathrm{p}$ is the particle flux, and $K_\mathrm{r}$'s are the reaction rate coefficients which appear in the source terms The fluxes are determined by the drift-diffusion approximation which results from the simplification of the momentum equation (ignoring inertia and convective terms)

$$\mathbf{\Gamma}_\mathrm{p} = \mathrm{sgn}(q_\mathrm{p}) \mu_\mathrm{p} \boldsymbol{E} n_\mathrm{p} - D_\mathrm{p} \nabla n_\mathrm{p}, \tag{4}$$

where $q_\mathrm{p}$ is the species charge, $\boldsymbol{E}$ is the electric field, and $\mu_\mathrm{p}$ and $D_\mathrm{p}$ are the transport coefficients of mobility and diffusion, respectively. When considering the electron energy evolution, the plasma is assumed to be weakly ionized and that electrons scatter primarily with a single dominant heavy particle species that comprises the background gas, which is assumed to be isothermal. Electrons are assumed to be in local thermodynamic equilibrium with a local temperature $T_\mathrm{e}$, mean energy $\varepsilon_\mathrm{e} = \frac{3}{2} k_\mathrm{B} T_\mathrm{e}$, and energy density $n_\varepsilon = n_\mathrm{e} \varepsilon_\mathrm{e}$ that is governed by the energy equation

$$\frac{\partial}{\partial t} n_\varepsilon + \nabla \cdot \mathbf{\Gamma}_\varepsilon = \mathbf{\Gamma}_\mathrm{e} \cdot q_\mathrm{e} \boldsymbol{E} - \frac{3}{2} \frac{m_\mathrm{e}}{m_\mathrm{g}} \nu_\mathrm{e} n_\mathrm{e} k_\mathrm{B} (T_\mathrm{e} - T_\mathrm{g}) - \sum_r H_\mathrm{r} K_\mathrm{r} n_\mathrm{e} n_\mathrm{r}. \tag{5}$$

The source terms include, in order, Joule heating, energy exchange through elastic scattering collisions, and energy lost or gained through reactions. New symbols introduced are the gas temperature and particle mass, $T_\mathrm{g}$ and $m_\mathrm{g}$, the electron momentum transfer collision frequency $\nu_\mathrm{e}$, and the change in energy per reaction $H_\mathrm{r}$. The electron energy flux is determined in the same manner as (4)

$$\mathbf{\Gamma}_\varepsilon = -\mu_\varepsilon \boldsymbol{E} n_\varepsilon - D_\mathrm{e} \nabla n_\varepsilon. \tag{6}$$

Finally, we separate the electromagnetic from the electrostatic response of the plasma. This is justified for the following of reasons: first, the time scale of the electromagnetism for the frequencies of interest are tens to hundreds of picoseconds, whereas the fluid response varies from tens of nanoseconds to microseconds. Second, the electromagnetic power used to interact with the plasma is assumed to be sufficiently small, generally microwatts or less, and so the electromagnetic power absorbed by the plasma is dwarfed by that of Joule heating from electrostatic-driven currents. Therefore, the fluid model we present treats the fields electrostatically through Poisson's equation with the inclusion free charges

$$\nabla^2\phi = -\frac{1}{\epsilon_0}\sum_p q_\mathrm{p} n_\mathrm{p}, \tag{7}$$

$$\boldsymbol{E} = -\nabla\phi. \tag{8}$$

*2.1.1. Boundary conditions.* The boundary condition on electrode surfaces consist of prescribing the particle flux for each species, similar to those used by others [31, 32]. For ions this is

$$\boldsymbol{\Gamma}_\mathrm{p}\cdot\boldsymbol{e}_\mathrm{n} = a\,\mathrm{sgn}(q_\mathrm{p})\mu_\mathrm{p}\boldsymbol{E}\cdot\boldsymbol{e}_\mathrm{n}\,n_\mathrm{p} + \frac{1}{4}v_\mathrm{p}n_\mathrm{p}, \tag{9}$$

where $\boldsymbol{e}_\mathrm{n}$ is the inward wall normal vector, $v_\mathrm{p}$ is the thermal velocity of the species, and the coefficient $a$ is one if $\mathrm{sgn}(q_\mathrm{p})\mu_k\boldsymbol{E}\cdot\boldsymbol{e}_\mathrm{n} > 0$ and zero otherwise. The boundary condition for electrons at electrodes has an additional term for secondary electron emission from ion impact, with the corresponding coefficient $\gamma$

$$\boldsymbol{\Gamma}_\mathrm{e}\cdot\boldsymbol{e}_\mathrm{n} = -a\mu_\mathrm{e}\boldsymbol{E}\cdot\boldsymbol{e}_\mathrm{n}\,n_\mathrm{e} + \frac{1}{4}v_\mathrm{e}n_\mathrm{e} - \gamma\boldsymbol{\Gamma}_\mathrm{i}\cdot\boldsymbol{e}_\mathrm{n}. \tag{10}$$

Lastly, the electron energy flux is similar to that of the electron particle flux

$$\boldsymbol{\Gamma}_\varepsilon\cdot\boldsymbol{e}_\mathrm{n} = -a\mu_\varepsilon\boldsymbol{E}\cdot\boldsymbol{e}_\mathrm{n}\,n_\mathrm{e} + \frac{1}{3}v_\mathrm{e}n_\mathrm{e} - \gamma\varepsilon_\mathrm{e}\boldsymbol{\Gamma}_\mathrm{i}\cdot\boldsymbol{e}_\mathrm{n}. \tag{11}$$

For non-electrode boundaries, such as symmetric or open boundaries, homogeneous Neumann conditions on particle densities are used. Boundary conditions on the electrostatic potential are either fixed at electrode surfaces or homogeneous Neumann type at symmetric or open boundaries. The typical simulation domain that we use is cylindrical with flat electrodes partially along grid boundary and is shown with boundary conditions specified in figure 1.

*2.1.2. Transport and rate coefficients.* The transport coefficients for electrons are found *a priori* via collision cross section data [33, 34] and a Boltzmann equation solver [20] that integrates the isotropic electron velocity distribution

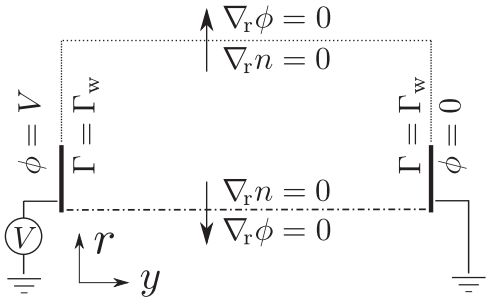


**Figure 1.** Simulation domain for pulsed experiments, consisting of two planar electrodes, symmetry boundary, and open boundaries.

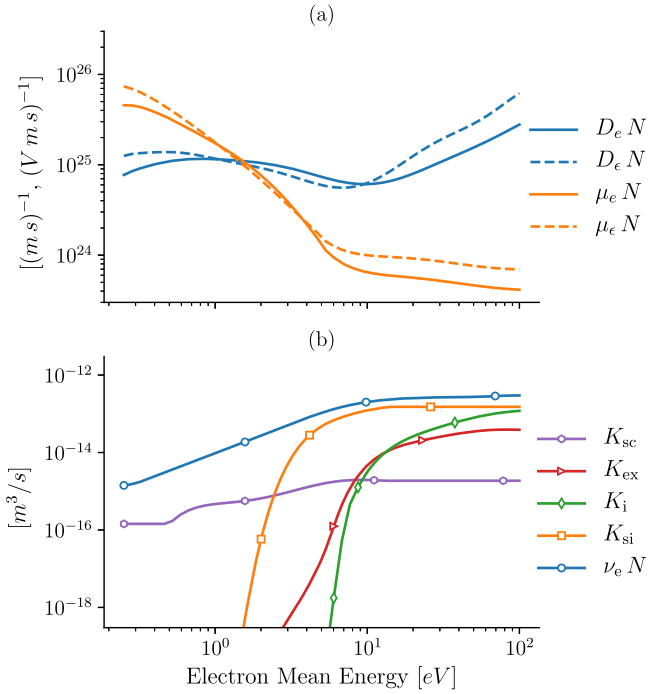


**Figure 2.** (a) Transport coefficients of electron particles (solid lines) and electron energy (dashed lines), and (b) rate coefficients in an argon plasma. Markers in (b) are for designation only, they do not represent datum locations.

function $F_0$ as

$$\mu_\mathrm{e}N = -\frac{\gamma}{3}\int_0^\infty \frac{\varepsilon}{\sigma}\frac{\partial F_0}{\partial\varepsilon}\,\mathrm{d}\varepsilon, \qquad D_\mathrm{e}N = \frac{\gamma}{3}\int_0^\infty \frac{\varepsilon}{\sigma}F_0\,\mathrm{d}\varepsilon,$$
$$\mu_\varepsilon N = -\frac{\gamma}{3\bar{\varepsilon}}\int_0^\infty \frac{\varepsilon^2}{\sigma}\frac{\partial F_0}{\partial\varepsilon}\,\mathrm{d}\varepsilon, \qquad D_\varepsilon N = \frac{\gamma}{3\bar{\varepsilon}}\int_0^\infty \frac{\varepsilon^2}{\sigma}F_0\,\mathrm{d}\varepsilon, \tag{12}$$

where $\sigma$ is the sum of all collision cross sections considered. These values are fitted to exponential functions for use during simulation for fast retrieval, and are shown in figure 2(a).

The rate coefficients for the argon excitation and ionization are found similarly from the Boltzmann equation solver [20] by integrating $F_0$ and the associated reaction cross sectional data over all electron energies as

$$K_\mathrm{r} = \gamma\int_0^\infty \varepsilon\sigma_\mathrm{r}F_0\,\mathrm{d}\varepsilon, \tag{13}$$

**Table 1.** Reactions considered in argon discharge for ionization, reactions with rate coefficients determined by $f(T_e)$ are shown in figure 2.

| Reaction | $H_m$ (eV) | $K_r$ ($m^3\ s^{-1}$) | References |
|---|---|---|---|
| $Ar + e \rightarrow Ar^* + e$ | 11.56 | $K_{ex} = f(T_e)$ | [20] |
| $Ar + e \rightarrow Ar^+ + e$ | 15.76 | $K_i = f(T_e)$ | [20] |
| $Ar^* + e \rightarrow Ar^+ + 2e$ | 4.14 | $K_{si} = f(T_e)$ | [17] |
| $Ar^* + e \rightarrow Ar + e$ | −11.56 | $K_{sc} = f(T_e)$ | [17] |
| $Ar^* + e \rightarrow Ar^r + e$ | — | $K_r = 2 \times 10^{-7}$ | [17] |
| $Ar^* + Ar^* \rightarrow Ar^+ + Ar + e$ | — | $K_{mp} = 6.2 \times 10^{-10}$ | [17] |
| $Ar^* + Ar \rightarrow 2Ar$ | — | $K_{2q} = 3 \times 10^{-15}$ | [17] |
| $Ar^* + 2Ar \rightarrow 3Ar$ | — | $K_{3q} = 1.1 \times 10^{-31}$ | [17] |

and the remaining rate coefficients are taken from [17]. The rate and transport coefficients used in our model for argon discharges are shown in figure 2(b), and the argon reactions are listed along with their associated energy in table 1.

The ion mobility is fixed at the beginning of the simulation, determined by the pressure law $\mu_i(p) = 0.145\, p^{-1}$ ($m^2\ V^{-1}\ s^{-1}\ Torr^{-1}$), and the diffusion coefficient is then related by the Einstein relation $D_i = \mu_i k_B/e$ [35].

### 2.2. Microwave response

We now describe our theoretical treatment of a microwave system to analyze the effectiveness of our simulated plasma discharges at controlling electromagnetic waves. As a sample system, we consider a resonant cavity that could be realized inside a photonic crystal or metallic waveguide, and for comparison with experiment we choose a rectangular cavity with dimensions $a = 1.58$ mm, $b = 7.9$ mm and $d = 13.7$ mm, in the Cartesian $x$, $y$, and $z$ directions, enclosed by reflective walls. A plasma column is aligned at the center of the $y$–$z$ plane and is situated along the $x$-axis. A schematic of the plasma inside the cavity is shown in figure 3. The empty cavity's lowest order mode corresponds to a transverse electric (TE) $(m, n, p) = (1, 0, 1)$ mode with a resonance frequency of

$$\omega_0 = \frac{\pi}{\sqrt{\mu\varepsilon}}\left(\frac{m^2}{a^2} + \frac{n^2}{b^2} + \frac{p^2}{d^2}\right)^{1/2} = 14.5\ \text{GHz}. \qquad (14)$$

The unfilled cavity is assumed to have a quality factor $Q_0 = 1900$, the ratio of the energy stored within the cavity to that lost per cycle, to match similar conditions seen in experiments [2]. When the cavity is partially filled with plasma, the local dielectric constant is determined by the Drude model, (1), and has the effect of increasing the resonance frequency of the cavity, $\omega_{res}$, with increasing plasma density. Furthermore, losses are introduced into the cavity due to the electron collision frequency and these losses will broaden the frequency response and reduce the quality factor of the cavity. Through perturbation theory the normalized resonance frequency shift, $\Delta\tilde{\omega}_{res} = (\omega_{res} - \omega_0)/\omega_0$, can be estimated from (appendix)

$$\Delta\tilde{\omega}_{res} = \left(1 - \frac{i+1}{Q_0} - \int_V \frac{\omega_p^2}{\omega_0^2 + i\nu_e\omega_0} E_0^2\, dV\right)^{\frac{1}{2}} - 1 \qquad (15)$$

by numerically integrating the field mode and plasma properties over the cavity volume, $V$. The primary assumption and limitation in this formulation is that the electric field profile, $E_0$, must be known and not greatly varied by the plasma, which is reasonable if the plasma's dielectric constant is near one. In this way, we make use of our simulated plasma density and collision frequency data in time and calculate measurable resonant frequency shifts. The electric field profile in the rectangular cavity is the lowest order mode

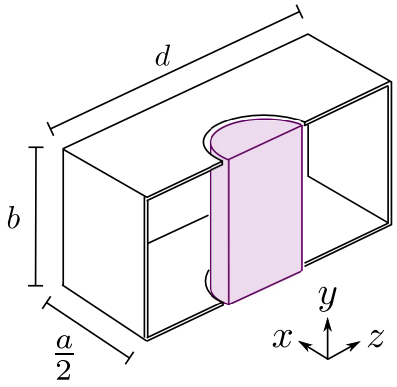


**Figure 3.** Schematic of a rectangular microwave cavity with a plasma column centered inside, the presence of which shifts the resonant frequency.

$$E_0(x, y, z) = \frac{2}{\sqrt{a\,b\,d}} \sin\left(\frac{\pi y}{a}\right) \sin\left(\frac{\pi z}{d}\right), \qquad (16)$$

and is defined according to the normalization condition, $\int E_0^2\, dV = 1$ (appendix). The quality factor of the filled cavity is determined by the ratio of real to imaginary parts of the solution to equation (15) as

$$Q = -\frac{1}{2}[1 + \text{Re}(\Delta\tilde{\omega}_{res})]\ \text{Im}(\Delta\tilde{\omega}_{res})^{-1}. \qquad (17)$$

If the cavity is thought to be coupling power from an input and output port, then the transmitted power through the cavity is also measurable and will vary with the excitation frequency $\omega$. In steady state, the normalized transmitted power, $T$, as a function of excitation frequency is given by [36]

$$T(\omega) = \left(\frac{1}{Q_0}\right)^2 \left[\left(\frac{\omega\ \omega_0^{-1}}{1 + \Delta\tilde{\omega}_{res}} - \frac{1 + \Delta\tilde{\omega}_{res}}{\omega\ \omega_0^{-1}}\right)^2 + \left(\frac{1}{Q}\right)^2\right]^{-1}, \qquad (18)$$

and so by calculating $Q_0$ and $\Delta\tilde{\omega}_{\text{res}}$, we may also calculate $T(\omega)$ and have a complete description of the plasma microwave system.

For slowly varying or quasi-steady systems this form of the transmitted power may be accurate, but for fast pulsing systems the Fourier domain response involves a frequency convolution between the natural response of the cavity and the dynamic response due to the pulsed plasma. In general there is no analytic solution such as (18), so we instead rely on treating the cavity as consisting of lumped circuit elements including a resistor, inductor, and capacitor as

$$L\frac{\mathrm{d}^2}{\mathrm{d}t^2}q \quad + \quad R\frac{\mathrm{d}}{\mathrm{d}t}q + \frac{q}{C} = P_0\sin(\omega t), \tag{19}$$

where $L$ is the inductance, $R$ is the resistance, $C$ is the capacitance, $q$ is the charge, $P_0$ is an arbitrary constant, and $\omega$ is the driving frequency. The circuit elements are related to the cavity properties by, $\omega_0^2 = (LC)^{-1}$ and $Q^{-1} = R(L\omega_0)^{-1}$, which we then use to rewrite the above equation as

$$\frac{\mathrm{d}^2}{\mathrm{d}t^2}q + \frac{\omega_0}{Q}\frac{\mathrm{d}}{\mathrm{d}t}q + \omega_0^2 q = \frac{P_0}{L}\sin(\omega_0 t). \tag{20}$$

If $\omega_0$ and $Q$ were stationary in time, then (20) is readily solved by taking the Laplace transform and finding the transfer function as the ratio between the input power, $P_0$, and output power, $P_1 \sim i^2 = \left(\frac{\mathrm{d}}{\mathrm{d}t}q\right)^2$, but as this is not the case we resort to numerical integration to calculate the frequency response.

Our modeling process is as follows: we first simulate a plasma discharge with our fluid model to retrieve the spatial (and temporal for pulsed discharges) variation in the electron density and collision frequency, then calculate the resonance frequency shift and reduced quality factor from (15) and (17). These two quantities are non-dimensional properties that are easily comparable to other experimental and numerical results, but perhaps are not as easily conceptualized. To remedy this, we lastly calculate the expected transmitted power spectrum by either using (18) directly for steady systems, or integrate (20).

### 2.3. Experimental setup

We have carried out experiments to validate our gas discharge simulations and our model of the electromagnetics. The experimental apparatus is a resonator device consisting of a WR62 rectangular waveguide section with two square metallic posts spaced 13.7 mm apart to create a resonant cavity [2]. In prior studies, we used this resonator in conjunction with an argon/mercury-filled cold cathode lamp to demonstrate microwave tuning and pulse formation. In this prior apparatus, interpretation of the data is difficult as the conditions and gas composition within the lamp are not known. In these new experiments described here, the resonator is enclosed in a vacuum chamber that is pumped to low pressures and backfilled with high purity argon gas to 2 Torr. The vacuum line is connected via a gate valve that is left cracked and a slow flow of argon gas is maintained through a needle valve so that the pressure is controlled and maintained while minimizing the effect of atmospheric air leaking into the chamber. A schematic of the experimental setup is shown in figure 4.

Continuous wave (CW) microwave signals are generated using an HP 8722D signal generator and are amplified to improve signal quality with an Hughes traveling wave tube (TWT) amplifier. The CW signal is passed through a 2.92 mm coaxial vacuum feedthrough into the chamber and is coupled to the WR62 resonator via waveguide to coaxial adapters. A 100 mm straight waveguide section is used after the adapter so that higher order waveguide modes are sufficiently damped before the electromagnetic wave encounters the resonator. The transmitted signal is coupled back to a coaxial cable via an adapter and passed out of the chamber before the power is measured using a crystal detector (Krytar 303S Zero Bias Schottky Detector). A 1 GHz Rhode & Schwarz RTE oscilloscope is used for data acquisition. The plasma is driven by a high voltage pulsed power supply, custom built by Airity Technologies, capable of pulse widths of 150 ns to supply high voltage pulses to flat tungsten electrodes that are 2 mm in diameter, isolated and flush with the upper and lower surfaces of the waveguide centered on the space between the resonator posts. An example voltage and current waveform recorded just outside of the vacuum chamber is shown in figure 5.

## 3. Results

Below we present representative results of discharge simulations of both quasi-steady state and transient plasma discharges suitable for controlling microwave propagation within the resonator of interest described above. Both simulations assume a background pressure of 2 Torr, a 2D cylindrical simulation domain of 7.9 mm by 7.9 mm, and electrodes 1 mm in radius along the centerline. The domain with boundary conditions is that shown in figure 1.

### 3.1. AC plasma discharge

To simulate a quasi-steady plasma discharge, the electrodes are supplied with a 500 kHz, ±350 V voltage source and the computations evolve through 32 AC cycles. Quasi-steady state is reached after approximately 25 cycles. Contours of electron particle density are shown at 64 $\mu$s in figure 6, which corresponds to when both electrodes are at 0 V. Also shown are the densities of electrons, ions, and metastable atoms along the centerline of the discharge. The electrode sheaths are clearly seen with a large region of charge separation between the ion and electron densities. The cathode sheath forms on alternating electrodes as the voltage oscillates, heats electrons up to high temperatures, and results in a locally high ionization. This accounts for the bright spots at both electrodes often seen in experiments. In figure 7 we show the current and voltage traces for several cycles during quasi-steady state.

The plasma column has a density on the order of $10^{17}$ m$^{-3}$, which corresponds to a plasma frequency of several GHz, and we expect this to behave as a positive epsilon dielectric column when immersed in electromagnetic structures with

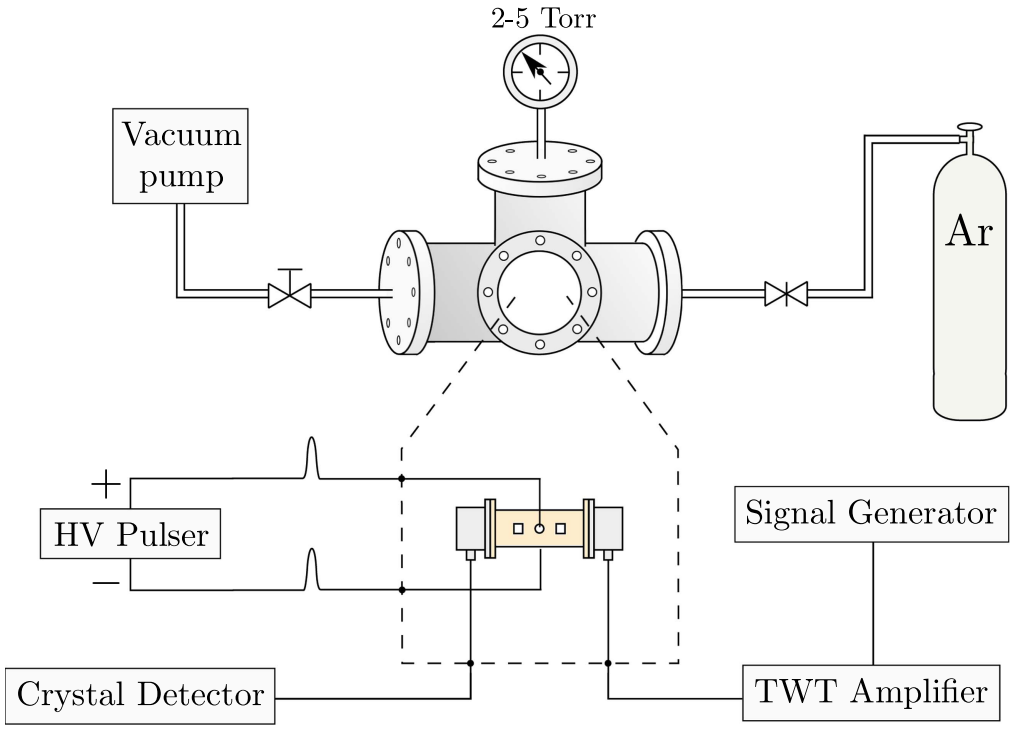


**Figure 4.** Setup of the microwave resonator experiments with a pulsed plasma discharge. The resonator is contained within a vacuum chamber and microwave signals generated by a signal generator and amplified by a TWT amplifier are coupled into and out of the chamber through coaxial cables and feedthroughs and detected by a crystal detector. A high voltage pulsed power supply generates the micro-plasma inside the waveguide using tungsten electrodes.

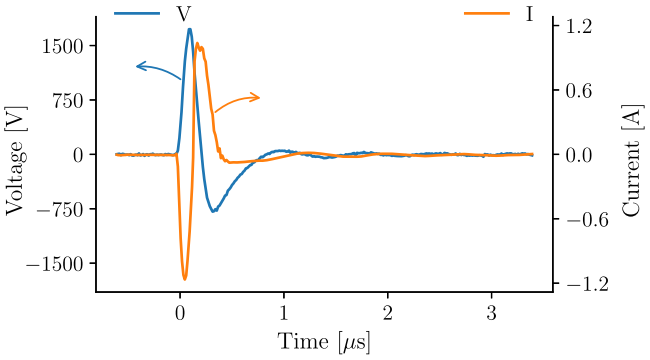


**Figure 5.** Typical current and voltage waveforms generated while driving a microdischarge in 2 Torr argon with an electrode separation distance of 7.9 mm.

wave frequencies of around 10 GHz. The microwave cavity response with the presence of this AC plasma is shown along with that of plasmas driven by similar conditions but with voltages of ±325 V, 335 V, and 350 V is shown in figure 8. At the lower discharge voltages (325 V and 335 V), the shifts in the transmission spectra relative to the empty resonator are less than 50 MHz and the Q of the filter is quite high ( 1900). With the 350 V discharge condition, the microwave cavity has a frequency shift of +125 MHz and the quality factor drops from 1900 to 430. This shows quite a large tunable range in steady state, and the transmission through the cavity with plasma is still easily measurable with only 12 dB of loss.

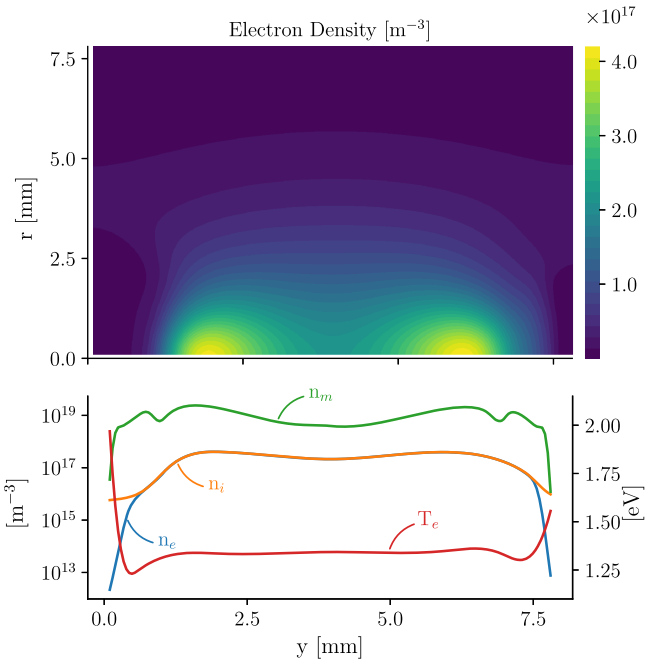


**Figure 6.** Electron density color-map along with the particle densities of electrons ($n_e$), argon ions ($n_i$), argon metastable atoms ($n_m$), and electron temperature ($T_e$) along the centerline of the plasma. Discharge is driven by a 700 $V_{pp}$ at 500 kHz voltage source in 2 Torr of argon.

### *3.2. Pulsed plasma discharge*

We also simulate transient plasma behavior with a pulsed plasma discharge using an experimentally measured voltage

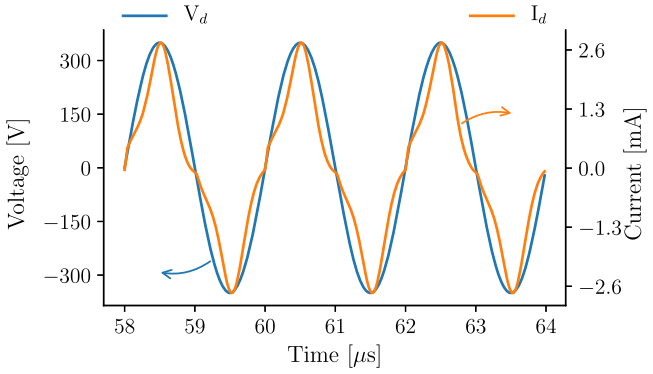


**Figure 7.** Discharge current and voltage waveforms of the voltage source driving a plasma at 2 Torr of argon with an electrode separation distance of 7.9 mm.

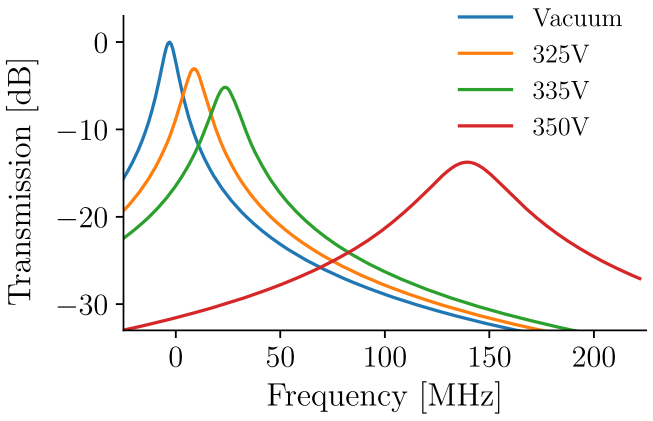


**Figure 8.** Microwave cavity transmission spectrum for the case of no plasma or with plasma driven by AC 500 kHz at ±325 V, 335 V, or 350 V.

waveform as input, shown in figure 5. The positive voltage peaks at 1780 V with a width of 150 ns width, and is followed by a negative voltage pulse peaking at −780 V with a 275 ns width. The ringing following the the two pulses has an amplitude of less than ±50 V and decays rapidly in a few cycles. The two pulses are used as the input condition for the fluid simulation, and the voltage waveform and resulting current waveform are shown in figure 9. The magnitude of the simulated discharge current is much lower than the experimentally measured current because they are not equivalent measurements; in fact most of the measured current pulse generated from the pulser unit is reflected back from the electrodes and is not easily quantified in the experiments.

Also shown in figure 9 are three dashed black lines that correspond to snapshots in time at which we show contours of electron density in figure 10, along with a plot of centerline particle densities of electron, argon ion, and argon metastable atoms, and electron temperature. The snapshots are located at 100 ns, 200 ns, 400 ns, and 5 $\mu$s, the last of which is long past the discharge voltage waveforms The first snapshot at 100 ns, shown in figure 10(a), corresponds to the first current spike and is a local ionization event at the anode that then propagates as an ionization wave towards the cathode. We have noticed that this ionization event occurs generally at the same

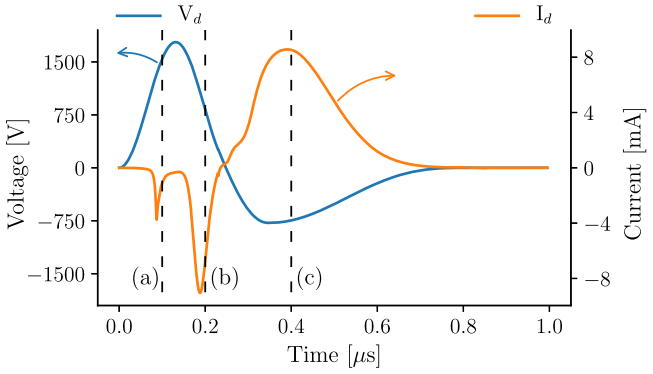


**Figure 9.** Current and voltage waveforms from a simulated pulsed plasma discharge in 2 Torr of argon with an electrode separation distance of 7.9 mm. Dashed lines correspond to snapshots in time shown in figure 10.

voltage regardless of the peak pulse voltage. Also, at the ionization front there is a region of charge separation, which is expected from an ambipolar drift wave.

There is a second current spike at 200 ns, with its associated snapshot shown in figure 10(b). This event is due to the formation of the cathode sheath (at $Y = 7.9$ mm) while the anode (at $Y = 0$ mm) is still at a positive voltage, the characteristic indicator of which is a region of large charge separation, which is confirmed in our centerline density plot. Locally high ionization accompanies the formation of the cathode sheath, and each of the particle densities peak at the cathode. This is seen both as a bright spot in the contour plot and as a peak in the centerline density plot of figure 10(b).

The largest discharge current peak occurs not during the positive voltage pulse but rather afterwards during the negative voltage pulse, shown in figure 10(c), for a couple of reasons: first, the plasma has already formed and has many more charge carriers, and second the negative voltage pulse is substantially wider than the positive pulse. The opposite polarity of the second pulse results in the cathode sheath switching sides and the region of large charge separation and high ionization is now seen at $Y = 0$ mm. Interestingly, the profile of the electron density is seen to peak along the centerline rather than be a diffuse glow around the electrode. After the two discharge voltage pulses, the plasma freely diffuses and recombines, and the fine structures are smoothed out over time. At 5 $\mu$s, shown in figure 10(d), there are still two distinct plasma blobs around the electrodes, but even these will coalesce over time as the plasma decays and becomes more diffuse.

*3.2.1. Microwave transmission.* The simulated plasma properties are used to calculate the microwave response of our resonant cavity in the presence of a pulsed plasma discharge. The fluid simulation advances to a time of 30 $\mu$s, after which we extrapolate frequency shift and quality factor to 300 $\mu$s. The predicted microwave transmission waveforms in time are shown in figure 11(a) for various microwave transmission frequencies given as $\Delta f = (\omega - \omega_0)/2\pi$ in MHz. We also conduct experiments at similar conditions to validate our predictions

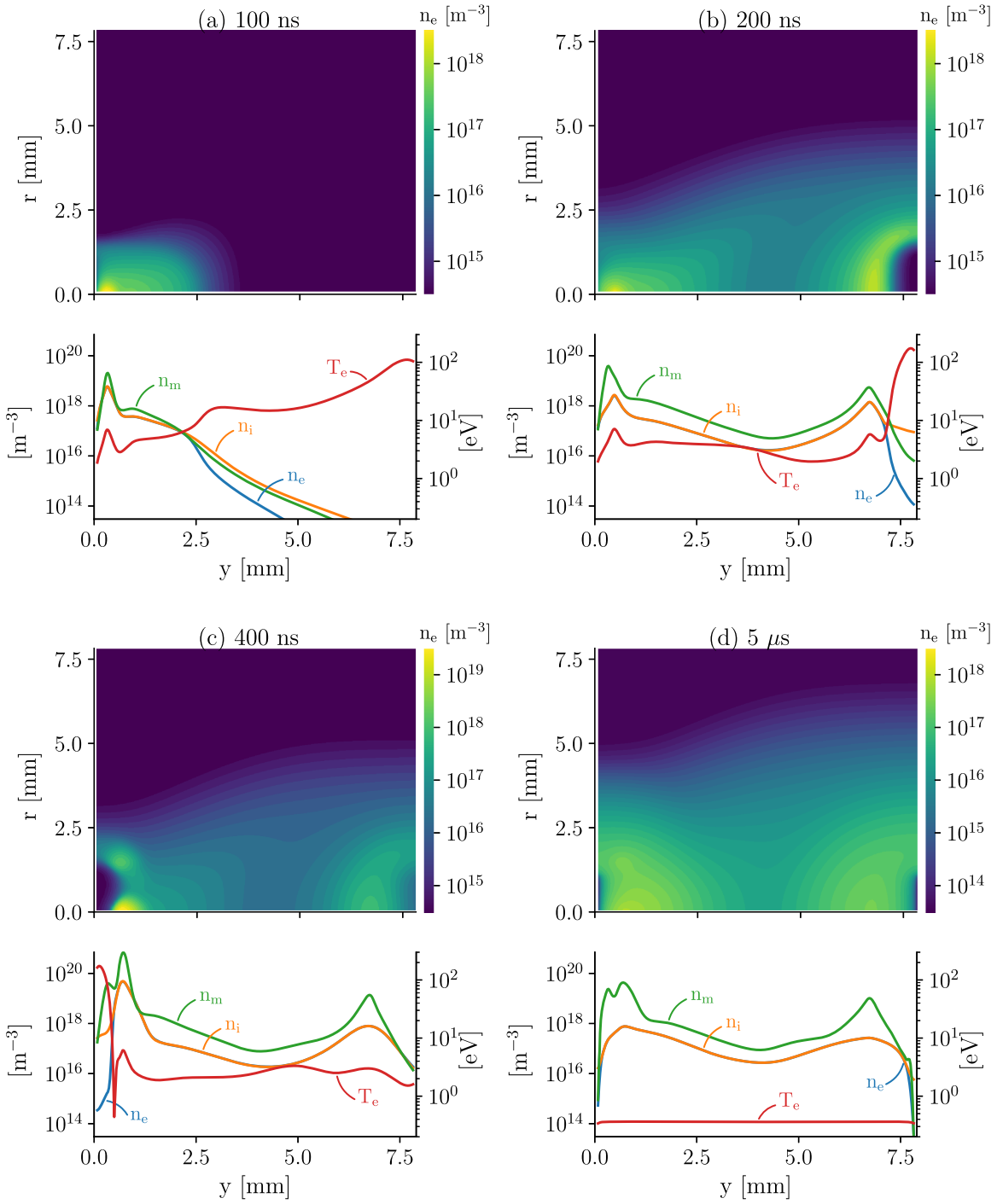


**Figure 10.** Contours of electron density at various snapshots in time, (a) 100 ns, (b) 200 ns, (c) 400 ns, and (d) 5 $\mu$s are shown along with particle densities of electrons ($n_e$), argon ions ($n_i$), metastable argon atoms ($n_m$), and electron temperature ($T_e$) are shown along the centerline of the plasma discharge. The plasma is driven by a voltage pulse, shown in figure 9, in 2 Torr of argon.

and include these results in figure 11(b). There is reasonable qualitative agreement between the predicted microwave pulses and their measured counterparts; for example in both plots the transmission curve for $\Delta f = 0$ MHz has full transmission before the plasma is ignited, drops rapidly with the discharge pulse around 20 dB, then recovers slowly over hundreds of microseconds. This is expected as only when the cavity is unfilled with plasma will there be transmission at the vacuum resonance frequency, and the transient dynamics of plasma ionization are much faster than plasma decay. The behavior of this mode of operation is sluggish and if used as a modulation technique would result in bandwidths of less than 10 kHz. On the other hand, as the transmission frequency is increased there is the formation of a microwave pulse that has a decreasing pulse width and delay time between the discharge voltage and the microwave pulse with further increases to the transmitting frequency. So much so, that by +80 MHz the simulated pulse width is 3 $\mu$s and the delay is 1 $\mu$s. Experimentally, we see that

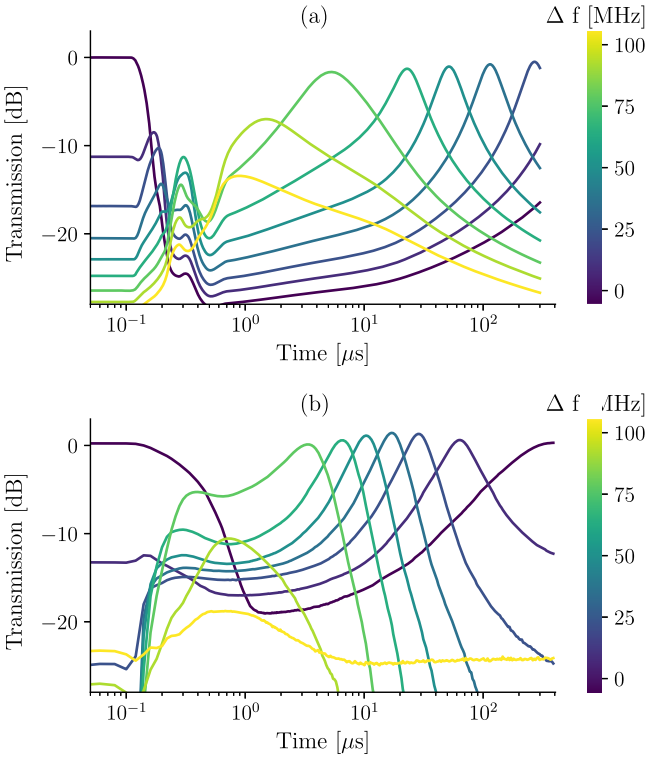


**Figure 11.** (a) Simulated and (b) experimentally measured microwave cavity transmission waveforms for various CW probe signal frequencies, given as $\Delta f = (\omega - \omega_0)/2\pi$ in MHz. The plasma was driven by a voltage pulse shown in figure 5 in 2 Torr of argon.

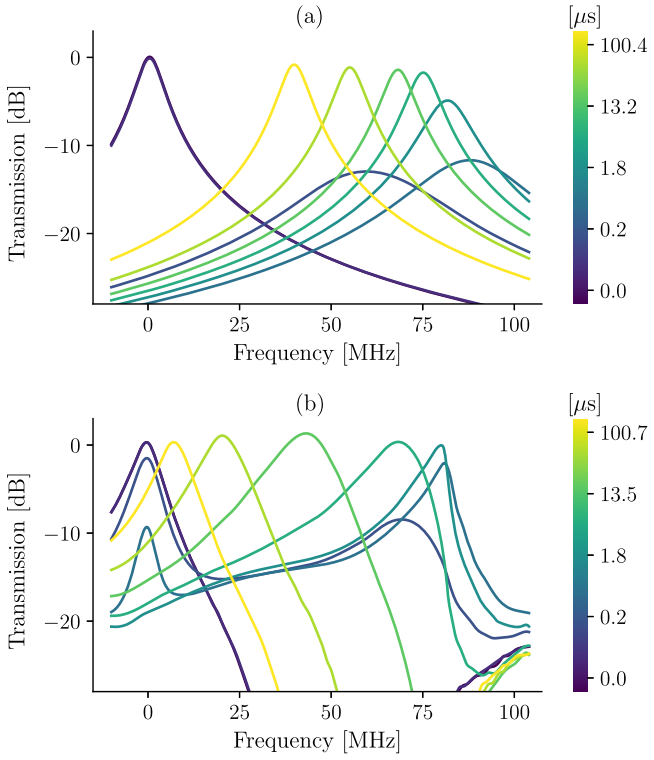


**Figure 12.** (a) Simulated and (b) experimentally measured microwave cavity transmission spectrums at various times during the plasma pulse. The plasma was driven by a voltage pulse shown in figure 5 in 2 Torr of argon.

the pulse width at the same frequency was as short as 1 $\mu$s, which would allow for bandwidths approaching 1 MHz. Thus by changing the transmission frequency by under half a percent, the maximum bandwidth is increased by two orders of magnitude.

Microwave pulses are formed in the plasma-cavity system when the plasma density changes in time and only when the resonance of the plasma-cavity system intersects the transmitting frequency will an output signal be seen. Higher transmission frequencies generate microwave pulses at earlier times because that is when the plasma density is also higher. The pulse widths depend on the rate of change of the plasma density inside the cavity, so we measure shorter microwave pulses at earlier times when the plasma is decaying more rapidly. On a logarithmic scale the pulse widths seem to be constant due to the exponential nature of plasma decay. Similar to the decaying plasma microwave pulses, we predict that there should be microwave pulses associated with plasma ionization, and in fact in our model results we see two sets of ionization pulses corresponding to the positive and negative voltage pulses of the discharge. These pulses have approximately the same pulse widths of 100 ns. However, we do not see the distinction between the two sets of ionization pulses in the experimental data but rather a merged microwave pulse, with widths of around 300 ns.

In general, our model does not capture the sluggish response of the cavity during plasma ionization, and underpredicts the decay rate of the plasma during recombination, resulting in an discrepancy of the microwave pulse delay widths. We attribute this partially due to the limitations of our analytic theory, especially the assumption that the field profile is constant. In the presence of non-uniformity in the plasma density, it should be the case that the electric field structure is varied to accommodate locally high density plasma. Since our analytic theory cannot account for this, a coupled electromagnetic simulation is required to fully capture the early dynamics of the plasma-wave interaction. Discrepancies in both pulse widths and delays are also attributed to uncertainty in the rate and transport coefficients used in our model, and more work on the fluid modeling is required to accurately resolve and correct this behavior.

Another way to visualize the transmission data is to view the reconstructed frequency response as a transmission spectrum at various times, and is shown for simulation in figure 12(a) and experiment in figure 12(b). As seen in both plots, the resonance shifts from its initial location to +80 MHz, the peak amplitude drops 10–15 dB, and the widths broaden substantially during the first 200 ns. From there, the peak amplitude recovers and the resonance frequency returns back to the origin. The simplified theory is evident here in that the modeled transmission responses are all Lorentzian in shape, whereas the experimentally measured responses do not have similarly long tails. Furthermore, other non-ideal features are present in the experimental data including a secondary resonance not associated with the cavity resonance at +100 MHz that is invariant in time. We verified the presence of this with a vector network analyzer, and confirmed its location and peak 25 dB lower than that of

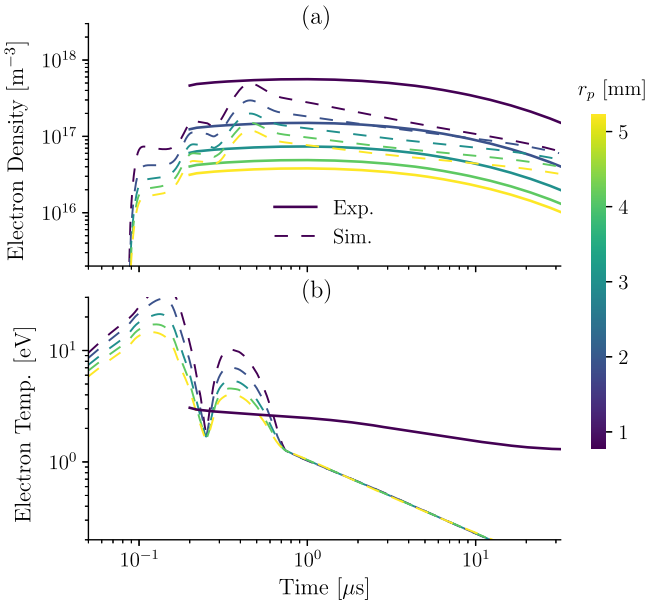


**Figure 13.** Estimated electron (a) densities and (b) temperatures are shown in solid lines, which were calculated using the experimentally measured microwave resonant cavity properties and assuming a uniform cylindrical plasma. The densities and temperatures are also compared to those obtained through our fluid simulation, shown in dashed lines corresponding to different radii of spatial averaging.

the primary cavity resonance. The secondary resonance interferes with the transmission spectrum of the cavity when the frequency is shifted nearby. However, we note that this is an experimental defect and would generally not be captured even in an electromagnetic simulation. Also, at the origin we see a spurious resonance even after plasma ignition, which is due to the fact that the cavity responds slowly to signals around its primary resonance as discussed earlier. Lastly, the predicted frequency response lags the experimentally measured response also due to earlier discussed uncertainties.

*3.2.2. Comparison with a uniform plasma.* As further validation of our models, we now present a comparison of our model results with an estimated electron density using the experimentally measured cavity properties. Specifically, we assume an uniform plasma cylinder centered in the cavity with various widths ranging from 1 to 5 mm in radius. We solve equations (15) and (17) for a range of electron densities and temperatures, then use that data to solve the inverse problem using a least-squares method to estimate the electron density and temperature for a given resonant frequency shift and quality factor. The resulting electron densities for the various radii are shown in figure 13(a) and similarly the electron temperatures in figure 13(b). Also shown in figure 13 are spatially averaged electron densities and temperatures from our fluid simulation in dashed lines for various assumed radii of averaging, similarly from 1 to 5 mm.

The estimated electron densities are all parallel in time and are shifted by a constant factor, with a spread of over an order a magnitude. This analysis also neglects the change in the effective plasma radius that will no doubt accompany an unconfined plasma discharge. Nevertheless, it is worth noting that for our conditions the assumption of a 2 mm radius uniform plasma seems to result in a reasonable representation of the simulated discharge over all time. However, since it is likely that such a finding is discharge condition specific, this result should not be used for predictive purposes, and illustrates the importance of developing and using discharge simulations for designing systems, since the plasma radius will not be known *a priori*.

The electron temperatures converged to the same curve for each plasma radius, which is perhaps an interesting if unexpected result. The agreement between the estimated and simulated electron temperature is poor, but this is relatively a less sensitive measurement due to the fact that the collision frequency does not vary as strongly in this range of temperatures. Furthermore, the measurement of the cavity quality factor in time has a larger uncertainty than the measurement of the frequency shift in time, so that the estimated electron temperature also has an expectedly larger uncertainty.

## 4. Conclusion

We have developed a fluid model to simulate plasma discharges for use in controlling electromagnetic waves and an accompanying analytic electromagnetic theory to evaluate the applicability of the simulated plasma discharges. We present results obtained using this model for quasi-steady state and transient plasma discharges and compared the electromagnetic response to experimental results obtained using similar conditions in a laboratory setting. There is good agreement between the peak frequency shift of 80 MHz, and the generation of microwave pulses ranging in widths of hundreds of microseconds to a few microseconds. We showed that changing the transmission frequency by less than 0.5% changes the bandwidth of such a microwave device by two orders of magnitude. While there is good qualitative agreement between the simulated and measured overall response, there are discrepancies in pulse delay width and time that are attributed to a number of limitations in the model and uncertainties in the rate and transport coefficients. Lastly, we compared our simulated electron density and temperature to those estimated using the experimentally measured resonant cavity properties and assuming a uniform cylindrical plasma. We see that there is again agreement, but the variance in the estimated densities is larger than an order of magnitude depending on the assumed plasma radius.

Future work includes studying the coupled electromagnetic response of the plasma-cavity system by solving the full set of Maxwell's equations. Such simulations can be used to explore other types of devices to prototype more complex plasma integrated systems for electromagnetic wave control such as plasma photonic crystals or plasma metasurfaces.

## Acknowledgments

This work was supported by the Air Force Office of Scientific Research (AFOSR) under Award No. FA9550-14-10317 through a Multi-University Research Initiative (MURI) grant titled Plasma-Based Reconfigurable Photonic Crystals and

Metamaterials with Dr Mitat Birkan as the program manager. We would like to thank Dr. Luke Raymond at Airity Technologies for his technical support with their high voltage pulsed power supply.

## Appendix. Resonant cavity theory

We now briefly show the effect of introducing plasma into a microwave resonator, following to the analysis of [36], in which they introduce three basis functions, two of which have zero divergence, $\boldsymbol{E}_a$ and $\boldsymbol{H}_a$, and one with zero curl, $\boldsymbol{F}_a$. The basis functions are also orthogonal and normalized over the cavity volume, $V$, as

$$\begin{aligned}\int_V \boldsymbol{E}_a \cdot \boldsymbol{E}_b \,\mathrm{d}V &= \delta_{ab},\\ \int_V \boldsymbol{H}_a \cdot \boldsymbol{H}_b \,\mathrm{d}V &= \delta_{ab},\\ \int_V \boldsymbol{F}_a \cdot \boldsymbol{F}_b \,\mathrm{d}V &= \delta_{ab},\end{aligned} \tag{A.1}$$

and can be used to expand field quantities, here shown for the electric field

$$\boldsymbol{E} = \sum_a \boldsymbol{E}_a \int_V \boldsymbol{E}\cdot\boldsymbol{E}_a \,\mathrm{d}V + \sum_a \boldsymbol{F}_a \int_V \boldsymbol{E}\cdot\boldsymbol{F}_a \,\mathrm{d}V. \tag{A.2}$$

Splitting the electric field into two terms is interpreted as differentiating the electromagnetic component from the $\boldsymbol{E}_a$ terms and the electrostatic component from the $\boldsymbol{F}_a$ terms It can be shown then that by using the above expansion, (A.2), that electromagnetic wave motion is described by the equation

$$\begin{aligned}&\varepsilon_0\mu_0\frac{\mathrm{d}^2}{\mathrm{d}t^2}\int_V \boldsymbol{E}\cdot\boldsymbol{E}_a \,\mathrm{d}V + k_a^2\int_V \boldsymbol{E}\cdot\boldsymbol{E}_a \,\mathrm{d}V\\ &= -\mu_0\frac{\mathrm{d}}{\mathrm{d}t}\left[\int_V \boldsymbol{J}\cdot\boldsymbol{E}_a \,\mathrm{d}V\right.\\ &\left. - \int_{S'} (\boldsymbol{e}_\mathrm{n}\times\boldsymbol{H})\cdot\boldsymbol{E}_a \,\mathrm{d}l\right] - k_a\int_S (\boldsymbol{e}_\mathrm{n}\times\boldsymbol{E})\cdot\boldsymbol{H}_a \,\mathrm{d}l.\end{aligned} \tag{A.3}$$

Here, $\boldsymbol{J}$ is the current density inside the volume and the last two terms correspond to Ohmic losses from surface currents (on surface $S'$) and energy radiating away through open boundaries (through surface $S$). Solutions to this equation are given to be of the form

$$\int_V \boldsymbol{E}\cdot\boldsymbol{E}_a \,\mathrm{d}V \sim \mathrm{e}^{\mathrm{i}\omega_\mathrm{res}t}, \tag{A.4}$$

where $\omega_\mathrm{res}$ is the complex resonance frequency. Furthermore, we now consider the volume to be dominated by the lowest order mode, $\boldsymbol{E}_a = \boldsymbol{E}_0$ with resonant frequency $\omega_0$. Equation (A.3) becomes

$$\begin{aligned}\omega_\mathrm{res}^2 - \omega_0^2 &= \mathrm{i}\frac{\omega_\mathrm{res}}{\varepsilon_0}\left(\int_V \boldsymbol{J}\cdot\boldsymbol{E}_0 \,\mathrm{d}V\right)\left(\int_V \boldsymbol{E}\cdot\boldsymbol{E}_0 \,\mathrm{d}V\right)^{-1}\\ &\quad - (\mathrm{i}+1)\frac{\omega_0^2}{Q_0},\end{aligned} \tag{A.5}$$

where we have grouped the loss terms on the right-hand side into $Q_0$ and used the wave relationship $k_0^2 = \varepsilon_0\mu_0\omega_0^2$. Next, we associate the currents within the cavity to electron fluxes, for which we use a simplified electron momentum equation

$$n_\mathrm{e}\frac{\mathrm{d}\boldsymbol{v}_\mathrm{e}}{\mathrm{d}t} = -\frac{\epsilon_0\omega_\mathrm{p}^2}{e}\boldsymbol{E} - \nu_\mathrm{e} n_\mathrm{e}\boldsymbol{v}_\mathrm{e}. \tag{A.6}$$

If we assume that the electron fluxes vary in time similarly to the cavity mode, that is their time dependence is proportional to $\exp(\mathrm{i}\omega_\mathrm{res}t)$, then the electron momentum equation can be rewritten as

$$\boldsymbol{J} = -en_\mathrm{e}\boldsymbol{v}_\mathrm{e} = \mathrm{i}\frac{\varepsilon_0\omega_\mathrm{p}^2}{\omega + \mathrm{i}\nu_\mathrm{e}}\boldsymbol{E}. \tag{A.7}$$

Using this form of the current density in (A.5) we have

$$\begin{aligned}\omega_\mathrm{res}^2 - \omega_0^2 = -\omega_0^2&\left(\int_V \frac{\omega_\mathrm{p}^2}{\omega_0^2 + \mathrm{i}\nu_\mathrm{e}\omega_0}\boldsymbol{E}\cdot\boldsymbol{E}_0 \,\mathrm{d}V\right)\\ &\times\left(\int_V \boldsymbol{E}\cdot\boldsymbol{E}_0 \,\mathrm{d}V\right)^{-1} - (\mathrm{i}+1)\frac{\omega_0^2}{Q_0},\end{aligned} \tag{A.8}$$

where we have made the approximation $\nu_\mathrm{e}/\omega_\mathrm{res} \approx \nu_\mathrm{e}/\omega_0$. Equation (A.5) is a quadratic equation for the angular resonance frequency of the cavity, $\omega$, and in general can be solved by assuming that the presence of currents within the cavity do not greatly affect the mode shape $\boldsymbol{E}_0$. We then approximate the expansion in (A.2) with $\boldsymbol{E} \approx \boldsymbol{E}_0\int\boldsymbol{E}\cdot\boldsymbol{E}_0 \,\mathrm{d}V$, resulting in

$$\Delta\tilde{\omega}_\mathrm{res} = \left(1 - \frac{\mathrm{i}+1}{Q_0} - \int_V \frac{\omega_\mathrm{p}^2}{\omega_0^2 + \mathrm{i}\nu_\mathrm{e}\omega_0}E_0^2 \,\mathrm{d}V\right)^{\frac{1}{2}} - 1. \tag{A.9}$$

Here, we have introduced a normalized frequency shift $\Delta\tilde{\omega}_\mathrm{res} = (\omega_\mathrm{res} - \omega_0)/\omega_0$. Equation (A.9) in general may be solved by numerically integrating a known plasma frequency profile and field mode profile over the cavity volume to calculate a frequency shift and damping factor.

## ORCID iDs

David R Biggs https://orcid.org/0000-0001-8230-2333

## References

[1] Semnani A, Venkattraman A, Alexeenko A A and Peroulis D 2013 Frequency response of atmospheric pressure gas breakdown in micro/nanogaps *Appl. Phys. Lett.* **103** 063102
[2] Biggs D R and Cappelli M A 2016 Tunable microwave pulse generation using discharge plasmas *Appl. Phys. Lett.* **109** 124103
[3] Sakai O, Sakaguchi T and Tachibana K 2007 Plasma photonic crystals in two-dimensional arrays of microplasmas *Contrib. Plasma Phys.* **47** 96–102
[4] Lo J, Sokoloff J, Callegari Th and Boeuf J P 2010 Reconfigurable electromagnetic band gap device using plasma as a localized tunable defect *Appl. Phys. Lett.* **96** 251501
[5] Wang B and Cappelli M A 2016 A plasma photonic crystal bandgap device *Appl. Phys. Lett.* **108** 161101

[6] Parsons S, Gregório J and Hopwood J 2017 Microwave plasma formation within a 2d photonic crystal *Plasma Sources Sci. Technol.* **26** 055002
[7] Lee D-S, Sakai O and Tachibana K 2009 Microplasma-induced deformation of an anomalous response spectrum of electromagnetic waves propagating along periodically perforated metal plates *Japan. J. Appl. Phys.* **48** 062004
[8] Sakai O and Tachibana K 2012 Plasmas as metamaterials: a review *Plasma Sources Sci. Technol.* **21** 013001
[9] Singh P K, Hopwood J and Sonkusale S 2014 Metamaterials for remote generation of spatially controllable two dimensional array of microplasma *Sci. Rep.* **4** 5964
[10] Raizer Y P 1991 *Gas discharge physics* ed J E Allen (Berlin: Springer)
[11] Hutchinson I H 2002 Principles of plasma diagnostics *Plasma Phys. Control. Fusion* **44** 2603
[12] Birdsall C K 1991 Particle-in-cell charged-particle simulations, plus Monte Carlo collisions with neutral atoms, pic-mcc *IEEE Trans. Plasma Sci.* **19** 65–85
[13] Pukhov A and Meyer-ter Vehn J 1996 Relativistic magnetic self-channeling of light in near-critical plasma: three-dimensional particle-in-cell simulation *Phys. Rev. Lett.* **76** 3975
[14] Hara K, Boyd I D and Kolobov V I 2012 One-dimensional hybrid-direct kinetic simulation of the discharge plasma in a Hall thruster *Phys. Plasmas* **19** 113508
[15] Filbet F, Sonnendrücker E and Bertrand P 2001 Conservative numerical schemes for the Vlasov equation *J. Comput. Phys.* **172** 166–87
[16] Boeuf J-P 1987 Numerical model of rf glow discharges *Phys. Rev.* A **36** 2782
[17] Lymberopoulos D P and Economou D J 1993 Fluid simulations of glow discharges: effect of metastable atoms in argon *J. Appl. Phys.* **73** 3668–79
[18] Subramonium P and Kushner M J 2002 Two-dimensional modeling of long-term transients in inductively coupled plasmas using moderate computational parallelism: I. Ar pulsed plasmas *J. Vac. Sci. Technol.* A **20** 313–24
[19] Houba T and Roy S 2015 Numerical study of low pressure air plasma in an actuated channel *J. Appl. Phys.* **118** 233303
[20] Hagelaar G J M and Pitchford L C 2005 Solving the Boltzmann equation to obtain electron transport coefficients and rate coefficients for fluid models *Plasma Sources Sci. Technol.* **14** 722
[21] Mitchner M and Kruger C H Jr 1973 Partially ionized gases
[22] Birdsall C and Langdon A B 2005 Plasma physics via computer simulation
[23] Gregório J, Parsons S and Hopwood J 2017 Reconfigurable photonic crystal using self-initiated gas breakdown *Plasma Sources Sci. Technol.* **26** 02LT03
[24] PanneerChelvam P, Raja L L and Upadhyay R R 2016 Computational modeling of a single microdischarge and its interactions with high frequency electromagnetic waves *J. Phys. D: Appl. Phys.* **49** 345501
[25] Levko D and Raja L L 2015 Early stage time evolution of a dense nanosecond microdischarge used in fast optical switching applications *Phys. Plasmas* **22** 123518
[26] Kourtzanidis K and Raja L 2017 Limitations of the effective field approximation for fluid modeling of high frequency discharges in atmospheric pressure air: application in resonant structures *Phys. Plasmas* **24** 112105
[27] Qu C, Tian P, Semnani A and Kushner M J 2017 Properties of arrays of microplasmas: application to control of electromagnetic waves *Plasma Sources Sci. Technol.* **26** 105006
[28] Hojo H *et al* 2004 Dispersion relation of electromagnetic waves in one-dimensional plasma photonic crystals *J. Plasma Fusion Res.* **80** 89–90
[29] Sakai O, Sakaguchi T and Tachibana K 2007 Photonic bands in two-dimensional microplasma arrays: I. Theoretical derivation of band structures of electromagnetic waves *J. Appl. Phys.* **101** 073304
[30] Arkhipenko V I, Callegari Th, Simonchik L V, Sokoloff J and Usachonak M S 2014 One-dimensional electromagnetic band gap structures formed by discharge plasmas in a waveguide *J. Appl. Phys.* **116** 123302
[31] Meunier J, Belenguer Ph and Boeuf J P 1995 Numerical model of an ac plasma display panel cell in neon–xenon mixtures *J. Appl. Phys.* **78** 731–45
[32] Veerasingam R, Campbell R B and McGrath R T 1997 One-dimensional fluid simulations of a helium–xenon filled ac colour plasma flat panel display pixel *Plasma Sources Sci. Technol.* **6** 157
[33] Yamabe C, Buckman S J and Phelps A V 1983 Measurement of free–free emission from low-energy-electron collisions with ar *Phys. Rev.* A **27** 1345
[34] Phelps A V 2014 The IST-LISBON database on LXCat *J. Phys.: Conf. Ser.* **565** 012007
[35] Smirnov B M 2008 *Reference data on atomic physics and atomic processes* vol 51 (Berlin: Springer) (https://doi.org/10.1007/978-3-540-79363-2)
[36] Slater J C 1946 Microwave electronics *Rev. Mod. Phys.* **18** 441